All-nanofiber–based, ultrasensitive, gas-permeable mechanoacoustic sensors for continuous long-term heart monitoring

Md Osman Goni Nayeem[a], Sunghoon Lee[a], Hanbit Jin[a], Naoji Matsuhisa[a], Hiroaki Jinno[a,b], Akihito Miyamoto[a], Tomoyuki Yokota[a], and Takao Someya[a,b,c,1]

[a]Department of Electrical Engineering and Information Systems, School of Engineering, The University of Tokyo, 113-8656 Bunkyo-ku, Tokyo, Japan; [b]Center for Emergent Matter Science, RIKEN, 351-0198 Wako, Saitama, Japan; and [c]Thin-Film Device Laboratory, RIKEN, 351-0198 Wako, Saitama, Japan

Edited by John A. Rogers, Northwestern University, Evanston, IL, and approved February 24, 2020 (received for review November 27, 2019)

The prolonged and continuous monitoring of mechanoacoustic heart signals is essential for the early diagnosis of cardiovascular diseases. These bodily acoustics have low intensity and low frequency, and measuring them continuously for long periods requires ultrasensitive, lightweight, gas-permeable mechanoacoustic sensors. Here, we present an all-nanofiber mechanoacoustic sensor, which exhibits a sensitivity as high as 10,050.6 mV Pa^{-1} in the low-frequency region (<500 Hz). The high sensitivity is achieved by the use of durable and ultrathin (2.5 μm) nanofiber electrode layers enabling a large vibration of the sensor during the application of sound waves. The sensor is ultralightweight, and the overall weight is as small as 5 mg or less. The devices are mechanically robust against bending, and show no degradation in performance even after 1,000-cycle bending. Finally, we demonstrate a continuous long-term (10 h) measurement of heart signals with a signal-to-noise ratio as high as 40.9 decibels (dB).

wearable electronics | biomedical devices | mechanoacoustic sensor | gas-permeable sensors

Enhancements of acoustic sensor sensitivities have extended their applications into the fields of communications, security, and healthcare/medicine (1–8). The recent emergence of wearable electronics has provided a strong motivation to further increase the sensitivity of acoustic sensors, particularly in the low-frequency regime, so as to enable the monitoring of low-intensity body acoustics normally beyond the audible range (1, 9). The frequency of heart signals is mainly concentrated in the 10–250-Hz band. Moreover, in the case of an impaired heart, the change in blood-flow velocity caused by myocardial contraction force variations, or by the incomplete closure of the valve mouth, result in tiny changes in the frequency and amplitude of the heart diastolic function (10, 11). Accurate monitoring of such activity over longer periods of time provides essential physiological and pathological information for the diagnosis of cardiovascular diseases (10, 12, 13).

Piezoelectric and triboelectric devices have a significant potential as wearable acoustic sensors, due to their high acoustic–electrical conversion efficiency and mechanical flexibility (14–23). The acoustic sensitivity of these devices has been significantly increased, simply through using nanofiber materials and/or modifying the geometric design of the substrate (24–27). For example, a polyvinylidene fluoride (PVDF) nanofiber-based acoustic sensor (28), with a centimeter-scale hole in the substrate, enabled the direct transfer of acoustic signals to PVDF nanofibers, and exhibited a maximum sensitivity of 266 mV Pa^{-1}. Furthermore, a triboelectric sensor (29), fabricated using a multiholed paper substrate with a hole diameter of 200 μm, has been reported in the literature. The porous structure of the substrate allowed for large vibrations of the sensor, resulting in a maximum sensitivity of 1,995 mV Pa^{-1}. In addition, triboelectric sensor (30) with a centimeter-scale cubic cavity exhibited a sensitivity as high as 9,540 mV Pa^{-1}, owing to the large compression/expansion of air inside the cavity.

For the accurate monitoring of small changes in bodily acoustic signals, the sensors have to be attached so as to minimize interference with the mechanoacoustic vibrations of the skin (9, 31–33). A skin-mounted accelerometer sensor, with an overall thickness of 2 mm, has been reported; it was capable of measuring the tiny skin vibrations caused by heartbeats (34). The 28-μm-thick PVDF film, sandwiched between two 47-μm-thick elastomers, can monitor seismocardiographic information without requiring an external power supply (35). Recently, a self-powered piezoelectric sensor (36), fabricated on an ultrathin plastic substrate (4.8 μm), was able to respond to a tiny human pulse, owing to a conformal attachment of the sensor on the skin surface; it exhibited an acoustic sensitivity of ∼250 mVPa^{-1}.

However, the achievement of high sensitivity in ultrathin sensors remains a challenge. Indeed, three-dimensional (3D) cavities, where the sound pressure is enhanced by resonance, can be used only for bulky sensors. In case of flexible acoustic sensors, the mechanical durability and thinness stand in a trade-off relationship. This is because a reduction in the thickness, and/or an introduction of pores in ultrathin substrates, make sensors fragile. The use of a thick protective film can improve the durability of the sensors; however, this also increases the overall thickness of the devices. Furthermore, when the substrates are porous and thin, the amplitude of vibration increases with respect to the same input, and thus a higher durability is required. The ultrathin porous substrates are susceptible to damage during handling, which makes it difficult to maintain the functionality of such devices for longer periods, particularly during long-term wearable operations.

Significance

We have fabricated an all-nanofiber–based mechanoacoustic sensor that exhibits an acoustic sensitivity as high as 10,050.6 mV Pa^{-1} in the frequency range of 10 to 500 Hz. The sensors are ultralightweight (total weight 5 mg or less) and gas-permeable. These superior performances enable our sensors to continuously measure the mechanoacoustic heart signals for longer periods (>10 h) with an extraordinarily high signal-to-noise ratio of 40.9 decibels.

Author contributions: M.O.G.N., S.L., H. Jin, N.M., H. Jinno, T.Y., and T.S. designed research; M.O.G.N., S.L., H. Jin, H. Jinno, A.M., and T.Y. performed research; M.O.G.N. contributed new reagents/analytic tools; M.O.G.N., S.L., N.M., T.Y., and T.S. analyzed data; and M.O.G.N., S.L., T.Y., and T.S. wrote the paper.

The authors declare no competing interest.

This article is a PNAS Direct Submission.

[1]To whom correspondence may be addressed. Email: someya@ee.t.u-tokyo.ac.jp.

This article contains supporting information online at https://www.pnas.org/lookup/suppl/doi:10.1073/pnas.1920911117/-/DCSupplemental.

First published March 18, 2020.

Here, we show an all-nanofiber mechanoacoustic sensor, which exhibits a sensitivity as high as 10,050.6 mV Pa^{-1}. This high sensitivity is realized by the fabrication of ultrathin (2.5 μm) nanofiber electrode layers, and forming a multilayered nanofiber sensor structure which enables a large vibration during the application of sound waves. Each of the layers being nanofiber structure, the effective mass density is significantly reduced and an overall weight as small as 5 mg or less is achieved. The sensors show an excellent gas permeability (12.4 kg-m^{-2}·d^{-1}) which is suitable for long-term wearable sensing applications. The nanofiber substrates are sufficiently durable, making the devices mechanically robust against repetitive bending (1,000 cycles), and show a stable operation of 27 h under continuous application of sound waves at very high intensity of 110 decibels (dB). Finally, a continuous long-term (10 h) measurement of mechanoacoustic heart signals with a signal-to-noise ratio as high as 40.9 dB demonstrates the practical applicability of our all-nanofiber sensors as wearable cardiac sensors.

Results and Discussion

The structure of the all-nanofiber mechanoacoustic sensor is shown in Fig. 1*A*. The sensor consists of three layers, i.e., bottom nanofiber electrode, PVDF nanofiber, and top nanofiber electrode layers, which were laminated together after each layer was separately manufactured. Scanning electron microscopy (SEM) images of each layer and the distribution of fiber diameters are shown in *SI Appendix*, Fig. S1. In order to fabricate the nanofiber electrode layer, a sheet of electrospun polyurethane (PU) nanofibers (with average fiber diameters of 650–950 nm) was transferred on the supporting frames with open windows. A 200-nm-thick parylene layer was deposited to improve the mechanical durability at the fiber-to-fiber joints (*SI Appendix*, Fig. S2). A 100-nm-thick Au electrode was deposited onto the PU nanofiber sheet through a shadow mask. A sheet of PVDF nanofibers (with average fiber diameters of 250–450 nm) was then prepared by a similar electrospinning method (*SI Appendix*, Fig. S3). In order to increase the piezoelectric conversion efficiency, bead-free PVDF nanofibers with smaller diameters were used, as discussed later in detail. The X-ray diffraction (XRD) pattern shows a peak at $2\theta = 20.2°$, which indicates PVDF nanofiber β-phase formation (*SI Appendix*, Fig. S4). The fabrication of the sensor was completed by sandwiching the PVDF nanofiber sheet between two nanofiber electrode sheets (*Methods* and *SI Appendix*, Fig. S5). Fig. 1*B* shows cross-sectional image of the all-nanofiber mechanoacoustic sensor obtained by SEM. The air gaps with typical spacings of 5–15 μm were naturally formed between the layers owing to the porous structure of the nanofibers. These gaps have an important role to achieve a high conversion efficiency, as discussed later. Fig. 1 *C* and *D* show the optical photograph and magnified surface 3D microscopic image of sensors, respectively. The sensor is ultralightweight with a total mass of 5 mg (or smaller) (*SI Appendix*, Fig. S6). Furthermore, owing to the porous structures of the nanofiber layers, the sensor exhibited an excellent water-vapor permeability of 12.4 kg-m^{-2}·d^{-1} (*Methods* and *SI Appendix*, Fig. S7). It is worth noting that no external power supply is required to generate a voltage signal under the application of a sound wave. All these features make the sensor suitable to be applied for continuous long-term monitoring of mechanoacoustic signals.

In order to evaluate the sensitivity, the output voltage generated by the sensor was monitored under the application of sound waves (*Methods* and *SI Appendix*, Fig. S8). The effective sensing area was 2.5 × 2.5 cm^2. When sound waves of 110 dB at 250 Hz were applied, a peak output voltage of 64 V was generated (Fig. 2*A*). The fast Fourier transform (FFT) of the generated output signal had a peak at 250 Hz, confirming that the output voltage was generated solely from the applied sound waves at 250 Hz

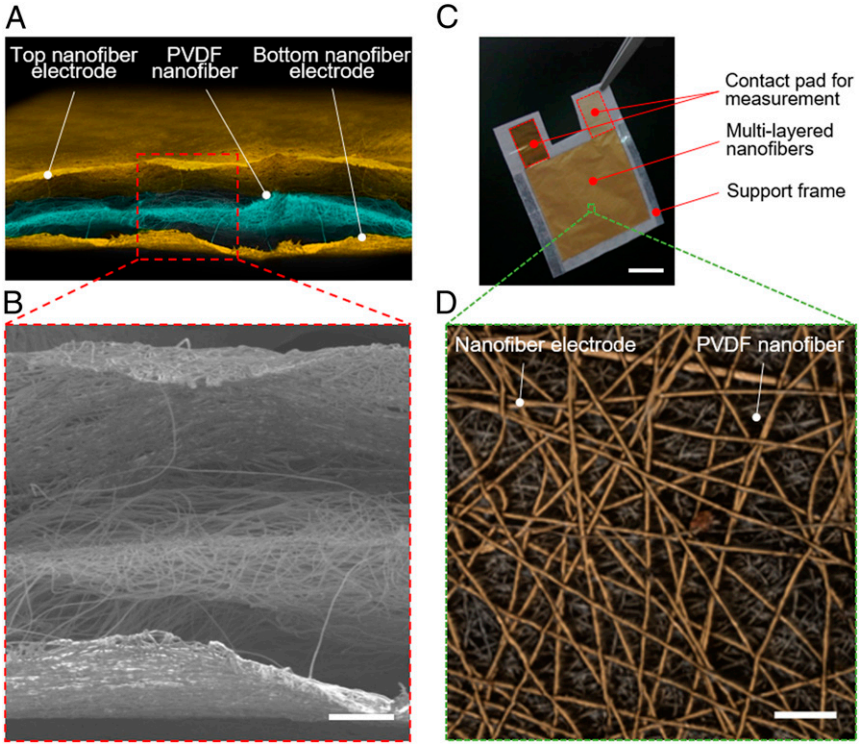

Fig. 1. Ultrasensitive all-nanofiber mechanoacoustic sensor. (*A*) Schematic of the all-nanofiber mechanoacoustic sensor. (*B*) Cross-sectional image of the sensor obtained by SEM. This image shows three layers, i.e., the bottom nanofiber electrode layer, the PVDF nanofiber layer, and the top nanofiber electrode layer. Air gaps naturally form between the layers, owing to the porous structure of the nanofibers. (Scale bar, 50 μm.) (*C*) Optical photograph of the fabricated sensor. (Scale bar, 1 cm.) (*D*) Surface 3D microscopic image of the sensor. (Scale bar, 30 μm.)

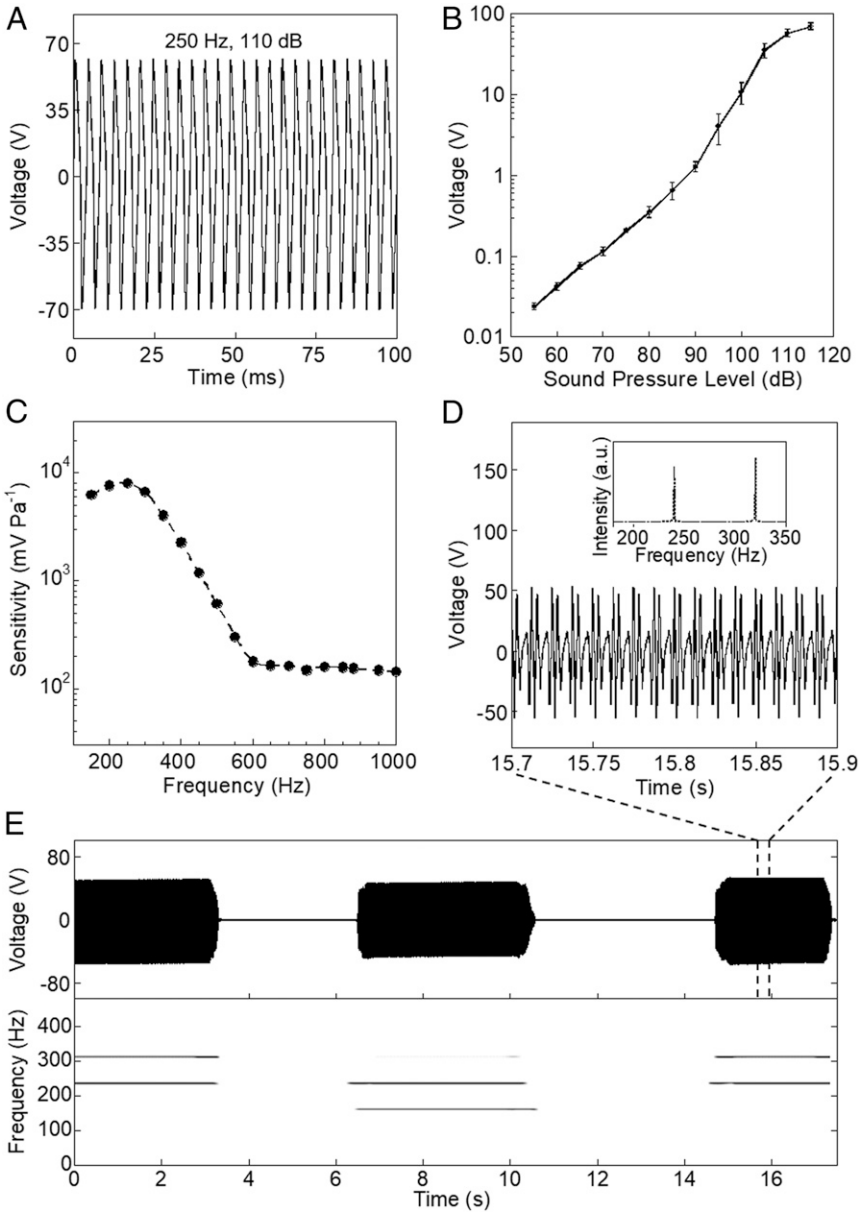

Fig. 2. Acoustic performance of the all-nanofiber mechanoacoustic sensor (*A*) Voltage waveform generated when a sound wave of constant frequency (250 Hz) and 110-dB SPL is applied to the sensor. The sensing area is 2.5 × 2.5 cm^2. (*B*) Effect of the SPL on the sensor performance ($n = 3$). (*C*) Frequency response of the sensor. (*D*) Bifrequency (240 and 320 Hz) detection when sound waves with two different frequencies are simultaneously applied to the sensor (*Inset*) Corresponding FFT of the two frequencies. (*E*) Sensor performance when sound waves with two different frequencies are simultaneously applied, and the corresponding spectrogram. The two different sound waves were simultaneously applied to the sensor in the following manner: 240 and 320 Hz (0–3.4 s), 160 and 240 Hz (6.5–10.5 s), and 240 and 320 Hz (14.5–17.3 s).

(*SI Appendix*, Fig. S9). The sound pressure level (SPL) was then changed at 250 Hz. When the SPL was increased from 55 to 115 dB, the peak output voltage significantly increased, from 24 mV to 70.9 V (Fig. 2*B*). The sensitivity at an SPL of 110 dB was as high as 9,229.8 mV Pa^{-1} (highest value: 10,050.6 mV Pa^{-1} at 105 dB), a high reported sensitivity of mechanoacoustic sensors. The high sensitivity (higher than 2,000 mV Pa^{-1}) was maintained even at a smaller SPL of 55 dB (*SI Appendix*, Fig. S10 and *Methods*). This makes our device particularly suitable for the measurement of low-intensity body acoustics, e.g., mechanoacoustic heart/lung signals due to the tiny nature of signal amplitudes.

In order to evaluate the frequency response, the frequency of the sound waves was changed at a constant SPL of 110 dB (Fig. 2*C*). The sensor exhibited a high-output response at the low-frequency region (<500 Hz); the maximum sensitivity was observed at 250 Hz. The sensitivity at the low-frequency region is very important for the measurement of body acoustics, in particular, for heart sounds, as their signals have frequencies of 10–300 Hz (11). In order to investigate the frequency resolution, sound waves generated by two different sound sources were applied to the sensors. Fig. 2 *D* and *E* show the electrical output signal and the corresponding spectrogram, respectively, when the sound waves with two different frequencies of 240 and 320 Hz (0–3.4 s), 160 and 240 Hz (6.5–10.5 s), and 240 and 320 Hz (14.5–17.3 s) were simultaneously applied to the sensor. The spectrogram exactly shows the two frequencies applied to the sensor at a certain time interval. A magnified view of the bifrequency signal is shown in Fig. 2*D*. The two peaks at 240 and 320 Hz are unambiguously

observed in the FFT (Fig. 2 *D*, *Inset*). Furthermore, the sensor could distinguish two sound waves with closer frequencies of 179 and 180 Hz (*SI Appendix*, Fig. S11).

An ultrahigh sensitivity of the sensor was achieved by a careful optimization of the structures and process parameters. We prepared two types of sensors for comparison: The same PVDF nanofiber sheets were sandwiched between nanofiber electrode sheets or continuous film sheets. The thickness of the nanofiber sheet was changed systematically from 9.4 to 2.6 μm, while that of the film sheet was changed from 10 to 1.5 μm (*Methods*). The output voltages and vibration amplitudes are shown in Fig. 3*A* as a function of the substrate thickness for both types of sensors. When the thickness of the nanofiber sheet decreased from 9.4 to 2.6 μm, the peak output voltage increased from 9.6 to 58.5 V, while the vibration amplitude increased from 250 to 415 μm. For the film-sheet–based sensor, the peak voltage increased from 670 mV to only 1.2 V, while the vibration amplitude increased from 81 to 299 μm when the sheet thickness decreased from 10 to 1.5 μm. Although the decrease in sheet thickness enabled a significant increase in vibration amplitude for both the nanofibers and film, the nanofiber-sheet–based sensor exhibited larger deformation and output voltage than those of the film-based sensor. These results are consistent with the previous reports on sensors and nanogenerators (16, 28, 29), where a larger deformation induced a larger voltage owing to piezoelectricity and triboelectricity. A simulation of the device vibration profile at a fixed sound is performed using COMSOL Multiphysics 3.5a (*SI Appendix*, Fig. S12).

We prepared all-nanofiber sensors with three different active layers: PVDF, PU, and polyvinyl alcohol (PVA) layers. Peak voltages of 58.5, 40.2, and 23.2 V were obtained for the PVDF, PU, and PVA nanofibers, respectively (Fig. 3*B*). It is reasonable that the PVDF nanofibers exhibited a larger peak voltage than those of the other two nanofibers owing to the piezoelectricity of PVDF. Ideally, if there are gaps between electrode layers and active layer, the piezoelectric signals cannot be generated. However, the nanofiber layers being extremely soft, there still exist few places where contact between the layers is maintained (*SI Appendix*, Fig. S13). Although the whole PVDF layer is not covered by Au-coated nanofiber layer, certain parts in contact contributed piezoelectric charge generation. Furthermore, it should be noted that the sensors with the nonpiezoelectric materials (PVA and PU) generated high voltages, induced by triboelectricity (37). Therefore, the large output voltage of the PVDF nanofibers can be attributed to the combination of piezoelectricity and triboelectricity where the triboelectricity is more dominant. In general, the sensitivity of piezoelectric sensors increases with the increase of frequency. But, in case of triboelectric sensors, natural frequency of sensors shifts due to the size of the sensor (30) because the resonance frequency is determined by the geometric structure. For this reason, the sensitivity of our device was decreased with the increasing frequency over 500 Hz.

In order to further investigate the triboelectric effect, a high-speed camera was employed to directly observe the vibrations of the sensors under the application of sound waves (*Methods*). Three different representative sensor states (bottom-contact position, neutral position, and up-contact position) under the application of sound waves are shown in Fig. 3*C*. It is worth noting that, as shown in Fig. 1, air gaps existed between the three layers of the sensors. Owing to air compression and rarefaction by the sound waves, the PVDF nanofiber layer oscillated between the top and bottom electrode layers (38, 39) (Movies S1 and S2). The large oscillation of the PVDF layer led to accumulation of opposite-polarity triboelectric charges on the Au-coated nanofiber and PVDF nanofiber layers, generating electric potential between the electrodes. These results show that the ultrahigh acoustic sensitivity of the all-nanofiber sensor can be attributed to the combination of piezoelectricity and triboelectricity, in addition to the nanoporous substrate. The high sensitivity at the low-frequency region is particularly important for biomedical applications. It is known that a high-frequency response can be achieved with a

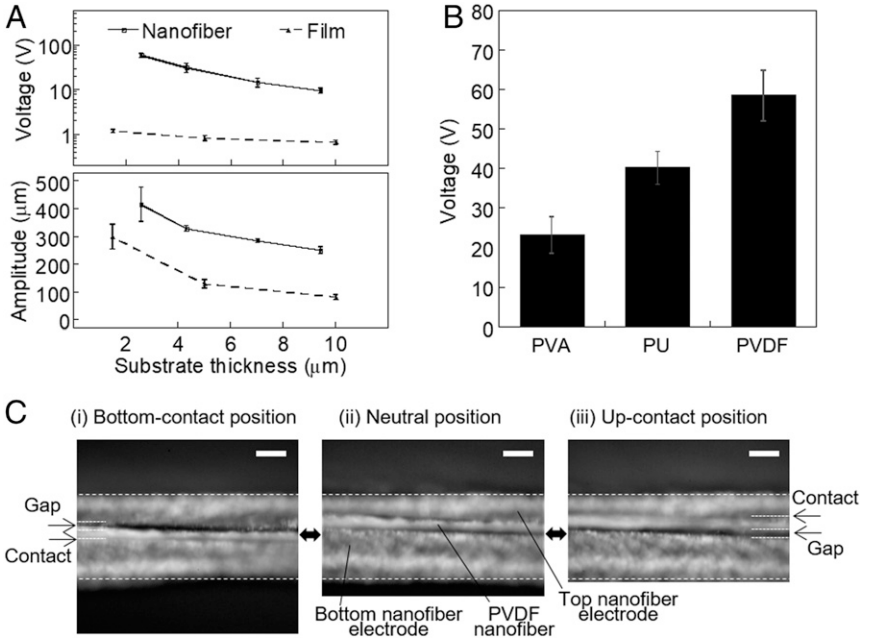

Fig. 3. Operation mechanism of the all-nanofiber mechanoacoustic sensor. (*A*) Effect of the substrate thickness on the output voltage (*Top*) and vibration amplitude (*Bottom*), and comparison of the all-nanofiber sensor against the ultrathin-film substrate sensor. Solid lines represent data for sensors with nanofiber substrate, and dashed lines represent sensors with the film substrate. (*B*) Output voltages of the sensors with various active layers (triboelectricity). Three different active layer materials, namely, PVA, PU, and PVDF are used. (*C*) Optical images of the sensors, showing three representative states: (*i*) bottom-contact position, (*ii*) neutral position, and (*iii*) up-contact position, under the application of sound waves (100 Hz), obtained by high-speed camera. (Scale bar, 30 μm.) The error bars represent the SD of the three samples.

microelectromechanical system (MEMS) sensor. However, the sensitivity of our sensor at the low frequency is significantly higher than those of MEMS sensors. For example, a diaphragm-free optical microphone (40) exhibited a sensitivity of 10.63 mV Pa^{-1} in the SPL range of 88–108 dB (0.5–5 Pa), while a triboelectric auditory sensor (41) for robotics or hearing aids exhibited a maximum sensitivity of 112.4 mV dB^{-1} or 513.9 mV Pa^{-1} in the SPL range of 85–110 dB.

Further, we evaluated the mechanical durability, which is important for the long-term operation of a wearable sensor. The output voltage was monitored while the sensor was bent from the flat state to a state with a bending radius of 6.5 mm. The change in the output voltage upon the bending was negligible (Fig. 4*A*). In order to further investigate the durability, a cyclic-bending experiment was performed with a bending radius of 6.5 mm. After 1,000 cycles, the change in the output voltage was negligible, showing the high robustness of the nanofiber sensor (Fig. 4*B*). This high robustness of our sensors is achieved due to the robust design of nanofiber electrode layers (*Methods*). We have tested the resistance changes of each nanofiber electrode layer against bending. The change in resistance is less than 2.2% while the nanofiber substrate was bent from the flat state (bending radius, ∞) to a state with a bending radius of 6.5 mm (*SI Appendix*, Fig. S14*A*). Additionally, in cyclic-bending test, after 1,000 cycles of bending with a bending radius of 6.5 mm, a maximum of 3.2% resistance change is observed (*SI Appendix*, Fig. S14*B*). Furthermore, the sensor exhibited a sufficient stability during the long-term operation. Indeed, after the continuous application of sound waves at the frequency of 250 Hz for 27 h with a high-pressure level (SPL of 110 dB), the change in the output voltage was smaller than 3% (*SI Appendix*, Fig. S14*C*).

Finally, the sensors were attached to a human chest, where they were positioned at the mitral valve for 10 h, to realize continuous seismocardiography, which is a measurement of the chest vibrations induced by heartbeats (*Methods*, Fig. 4*A*, and *SI Appendix*, Fig. S16). The signals were measured for 5 min at intervals of 1 h. As these vibrations are very small, their detection requires ultrasensitive and ultralightweight sensors (34, 42). The frequency of the signals of a normal heart is predominantly concentrated in the 20–150-Hz band. The changes of frequency or amplitude in heart signals provide information about imparity in the heart, caused by changes in the myocardial contraction forces or heart blood-flow velocity (10). Therefore, the continuous long-term monitoring of heart signals is important to clinicians, enabling them to observe such changes in frequency or amplitude, and subsequently to diagnose heart diseases more effectively. The heart signals measured by our sensors, and the corresponding spectrograms, show that the frequency of the heart signals of the human subject also lie in the normal frequency band throughout the course of the 10-h experiment. The stable monitoring of the heart rate (in beats per minute, BPM) was performed over a period of 10 h (Fig. 4*B*). The signal-to-noise ratio (SNR) was as high as 38.2–40.9 dB during the measurement procedure, which is a significant improvement compared to the recent reports of mechanoacoustic sensors (34, 35). This high SNR value over 10-h measurement shows the feasibility of the all-nanofiber–based gas-permeable mechanoacoustic sensors for continuous long-term heart monitoring applications. Finally, a comparison of the data obtained with our all-nanofiber sensor and a commercial cardiac microphone over a 30-min period, and a magnified plot of this comparison, are shown in Fig. 5 *D* and *C*, respectively. The results show that our sensor can measure the tiny mechanoacoustic heart signals, with a quality comparable to that of a commercial medical-grade cardiac microphone.

Conclusions

We have reported the design of an all-nanofiber, ultrasensitive, ultralightweight, gas-permeable mechanoacoustic sensor. The all-nanofiber sensors show a superior acoustic sensitivity in the low-frequency region, and at the same time maintain high mechanical robustness and stability under bending. The continuous 10-h seismocardiographic measurements show our sensor's superiority as a mechanoacoustic sensor for long-term cardiac monitoring. In the future, integration of nanomesh electrocardiogram (ECG) electrodes, along with our all-nanofiber sensor, will enable the long sought-after inflammation-free, long-term simultaneous monitoring of ECG and SCG. Utilizing the ultrahigh sensitivity in high sound-pressure region might open up application opportunities of our sensor in voice-controlled security for next-generation human–machine interface (HMI) and environmental noise sound harvesting.

Methods

Preparation of the Nanofiber Substrate. The nanofiber substrate was fabricated by modifying the previously reported method (43, 44). A PU solution (Rezamin M-8115LP, Dainichiseika) was diluted to obtain a 15 wt % solution with a mixed solvent [N, *N*-dimethylformamide (DMF):methyl ethyl ketone with a ratio of 7:3], and subsequently stirred at room temperature for 2 h. The PU nanofiber sheet was prepared by far-field electrospinning (Fuence ES-2000). The PU solution was placed in a glass syringe with a metallic needle (27 G) maintaining the distance of 15 cm between the needle tip and the grounded collector. The solution was injected at a flow rate of 10 μL min^{-1} under an applied voltage of 20 kV for 5 min. The electrospun PU nanofiber sheet was then transferred to a 1-μm-thick parylene support film with a window. The 1-μm-thick parylene support film was prepared on a 125-μm-thick

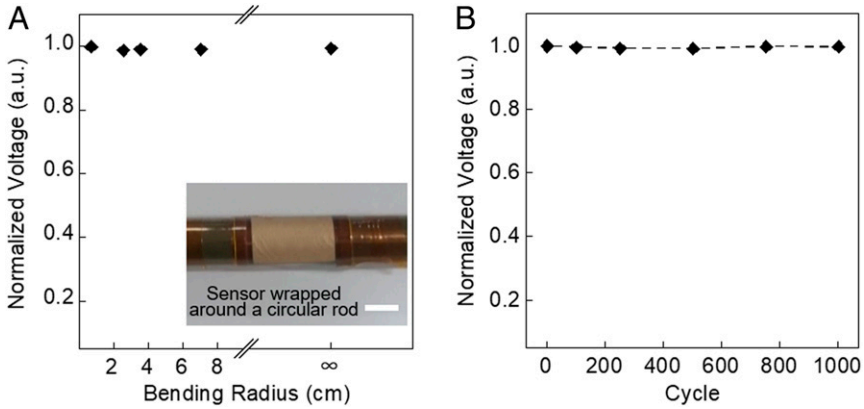

Fig. 4. Mechanical characteristics of all-nanofiber mechanoacoustic sensor. (*A*) Output voltage performance at different bending radii, ranging from the flat state (∞) to a 6.5-mm bending radius (*Inset*) Optical photo of the sensor in bending state. (Scale bar, 1 cm.) (*B*) Cyclic durability of up to 1,000 repetitive bending cycles.

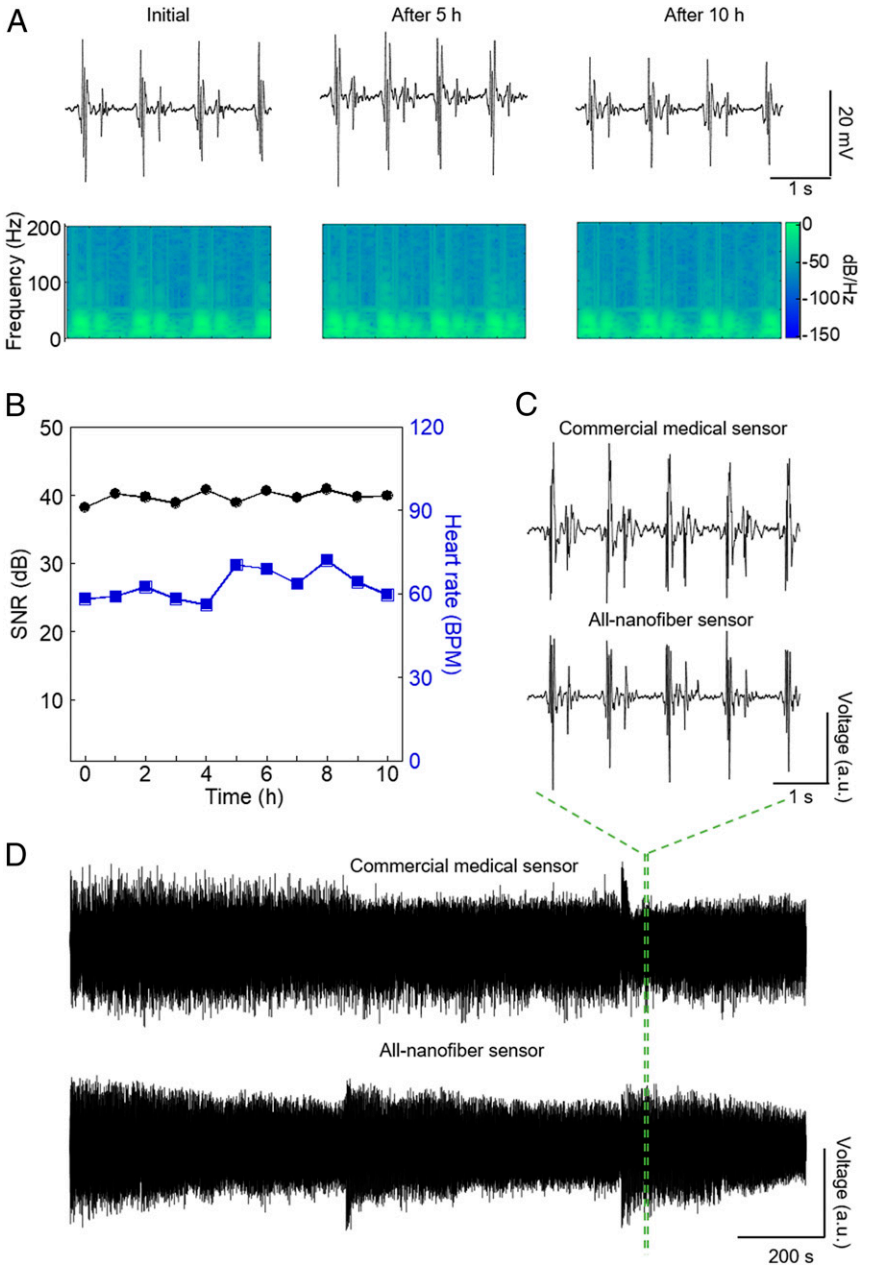

Fig. 5. Continuous monitoring of heart signals (seismocardiography) using the all-nanofiber mechanoacoustic sensor. (*A*) Heart signals (initial, after 5 h, and after 10 h), and the corresponding spectrograms. (*B*) SNR and heart rate in BPM during the 10-h experimental period. The black curve represents the SNR, and blue represents the BPM. (*C* and *D*) Comparison of the heart signals measured by a commercial cardiac microphone and an all-nanofiber sensor. Heart signals were measured continuously for 30 min. (*D*) A magnified version of the signals in *C*.

polyimide (PI) film by chemical vapor deposition. The PI film was used as a temporary substrate during the fabrication; a fluorinated polymer was spin-coated as a sacrificial layer on top of the PI film. A window was fabricated on the parylene/PI substrate with dimensions of 2.5 × 2.5 cm^2, and then the PU nanofiber sheet was transferred onto the parylene/PI substrate. Within this window, the PU nanofiber sheet was freestanding, while in the other regions, the nanofibers were supported by the parylene/PI substrate. A 200-nm-thick parylene layer was then coated around each PU fiber to enhance the strength of the fiber-to-fiber joints. The nanofiber electrode preparation was completed by depositing a 100-nm-thick Au layer with a shadow mask using a thermal evaporator. The average sheet resistance for our nanofiber electrode layers was 2.293 ± 0.069 Ω. The sheet-resistance measurement was performed with a four-point probe measurement system (model ∑-5+, NPS Inc.). The contact pad is directly formed on parylene-coated PU fibers supported on top of the 1-μm parylene film as shown in Fig. 1*C*.

Preparation of the PVDF Nanofiber Sheet. The PVDF nanofiber sheet was fabricated by a similar electrospinning process (Fuence ES-2000). PVDF pellets (molecular weight: 275,000 g mol^{-1}, Sigma-Aldrich) were dissolved in a mixed solvent (DMF:acetone with a mixing ratio of 4:6 v:v) and stirred at 70 °C for 3 h to prepare a 19 wt % PVDF solution. The solution was then placed in a glass syringe with a metal needle (27 G). Electrospun nanofibers were collected on a silicone-coated paper placed on top of a grounded flat collector. The distance between the metal needle tip and the grounded collector was maintained at 15 cm; fibers were drawn to fabricate the PVDF nanofiber sheet. Three parameters of the electrospinning process (solution concentration, applied voltage, and flow rate) were investigated to optimize the PVDF nanofiber formation. The solution concentration was in the range of 15–23 wt %, the applied voltage was in the range of 15–30 kV, and the flow rate was in the range of 5–15 μL min^{-1}. As shown in *SI Appendix*, Fig. S3 *A–C*, at a concentration of 15 wt % (constant voltage of 20 kV and flow rate

of 10 μL min^{-1}), the PVDF fibers contained a large number of beads, although the average diameter was smaller. With the increase in the solution concentration, the beads disappeared, while the average fiber diameter significantly increased. At the applied voltage of 15 kV (constant concentration of 19 wt % and flow rate of 10 μL min^{-1}), the fibers became thicker and contained beads, as shown in *SI Appendix*, Fig. S3 *D–F*. With the increase in the applied voltage, the fibers became thinner. However, at a too-high voltage over 30 kV, the solvents instantly evaporated and caused clogging at the needle tip. *SI Appendix*, Fig. S3 *G–I* show the effect of the flow rate, where the fiber diameter increases with the introduction of some beads in the fibers when flow rate is increased. Therefore, the optimized electrospinning for the PVDF nanofiber sheet formation involved a solution concentration of 19 wt %, an applied voltage of 20 kV, and a flow rate of 10 μL min^{-1}. During electrospinning, in situ stretching and poling occurs during fiber drawing with the application of high voltage (20 kV). Due to this in situ stretching and poling, PVDF nanofiber change its phase into polar β-phase from α-phase which can be known from XRD analysis (*SI Appendix*, Fig. S4).

Characterization of the Nanofibers. The morphologies of the nanofibers (both PVDF and PU nanofibers) were analyzed by SEM (Hitachi S-4800, FE-SEM). The SEM images were used to estimate the fiber diameter using an image processing software (ImageJ 1.50b).

The out-of-plane XRD pattern of the PVDF nanofibers mounted on a glass holder was obtained using a Rigaku SmartLab diffractometer. The sample was scanned in the range of 10° to 60° at a scan rate of 0.2° s^{-1} with a measurement step of 0.02° in a 2θ–θ configuration with a Cu-K_α source (λ = 1.541 Å) at 40 kV and 30 mA.

Fabrication of the Mechanoacoustic Sensors. The mechanoacoustic sensors were fabricated by sandwiching a PVDF nanofiber sheet between two (top/bottom) electrode substrates. After each layer is manufactured separately, three layers were laminated together, and a heat and press (50 °C and 200 N) is applied for 1 min to complete the fabrication of sandwich structure of the sensors. The three layers are laminated together intending to achieve a freestanding triboelectric sensor configuration.

1) Nanofiber substrate. The thickness of the nanofiber substrate was controlled by varying the electrospinning time in the range of 5–20 min. The thickness was measured using a color 3D laser scanning microscope (KEYENCE, VK-9710).
2) Uniform parylene film substrate. The ultrathin parylene substrate was prepared by depositing a 1.5-μm-thick parylene on a 125-μm-thick PI substrate. The PI film was used as a temporary substrate during the fabrication. A fluorinated polymer was spin-coated as a sacrificial layer on top of the PI film. Thin parylene film substrates with three different thicknesses (1.5, 5, and 10 μm) were prepared.

In each case, the PVDF nanofiber sheet thickness was constant (6–7 μm).

Characterization of the Sensors. The measurement setup for the acoustic sensor characterization consisted of a loudspeaker connected to a personal computer, as a sound source. The distance between the sound source (speaker) and the sensor is maintained to be 1 cm throughout the experiments. The SPL is varied by varying the volume of speaker from the computer. The SPL was measured using a sound-level meter (SL8850). The corresponding electrical output signal was measured using an oscilloscope (KEYSIGHT InfiniiVision DSOX4024A). Cu wires were used as wirings, attached to the Au pads on the parylene support film of the sensor. During the characterization, the sensor was firmly attached to a fixed frame. In order to avoid false vibration of the equipment, the frames were supported by a heavy slabstone base.

The vibration amplitudes of the sensors were measured using a laser displacement sensor (KEYENCE, LE-4000). A schematic of the vibration setup is shown in *SI Appendix*, Fig. S15. Sounds were applied using a loudspeaker from the bottom side of the sensor and the laser was pointed at the center of the top surface of the sensor to measure the vibration amplitude.

A high-speed camera (Phantom v711) was used to analyze the real-time vibration and the contact–separation between the layers of the sensor. The sample was prepared by cutting the sensor at one edge using ultrasharp scissors. The sample was placed on a sample holder so that the cut edge of the sensor faced the camera lens. Sound waves (frequency of 100 Hz and SPL of 110 dB) were then applied from the bottom side of the sensor and the corresponding vibration as well as the contact–separation between the layers were recorded. The movies were acquired at a frame rate of 1,000 frames per second.

Calculation of the Sensitivity. The sensitivity (S) of the acoustic sensor was calculated by

$$S = \frac{V}{P} = \frac{V}{P_0.10^{SPL/20}}, \quad [1]$$

where P is the sound pressure, V is the peak output voltage of the sensor, and P_o is the reference sound pressure of 2×10^{-5} Pa; the SPL is expressed in dB.

Gas-Permeability Test. Three bottles were used for the experiment; each of them contained 1 g of water. The all-nanofiber mechanoacoustic sensor and the 5-μm-thick parylene film coated with Au were attached to the openings of the two bottles, while the third bottle was kept open. The water vapor permeability was estimated by measuring the weight loss of water. The samples were stored in a thermostatic chamber at a temperature of 25 °C and a humidity of 30%. The weights of the bottles were measured after every 24 h for 6 d.

Water-vapor permeability (WVP) in kg $m^{-2}{\cdot}d^{-1}$ was calculated according to the following equation:

$$WVP = \frac{m_1 - m_2}{S} \times 24, \quad [2]$$

where m_1 and m_2 are the bottle weight before and after test, respectively, and S is the opening area of the bottle.

Seismocardiography. The seismocardiography was carried out by attaching the sensors at the mitral valve position of the human chest. An ultrathin transparent film dressing (3M Tegaderm) with a window of the same size as the sensing area was used to attach the sensor to the chest. Due to the window of Tegaderm film, the natural movements and gas permeability of the skin are not hindered during the monitoring of heart signals. Data were recorded at a sampling rate of 1 kHz using a Neuropack ×1 (NIHON KOHDEN MEB 2300). The subject was comfortably seated on a chair with a backrest support. The signals were measured with a bandpass filter (10–500 Hz) and a notch filter (50 Hz). The ratio between the peak-to-peak voltage of the signal and the peak-to-peak voltage of the noise region was used to calculate SNR. The study protocol was thoroughly reviewed and approved by the ethical committee of The University of Tokyo (approval number KE18-14).

Data Availability. All data supporting the findings of this study are either included within the paper or available from the corresponding author upon request.

ACKNOWLEDGMENTS. This work was financially supported by the Japan Science and Technology ACCEL (Grant JPMJMI17F1), Japan. M.O.G.N. was supported by World-leading Innovative Graduate Study Program innovations for Future Society. The authors would like to express their gratitude to Dr. David D. Ordinario, Dr. Robert A. Nawrocki, and Dr. Simiao Niu for helpful scientific discussions and technical advice.

1. K. W. Beach, B. Dunmire, "Medical acoustics" in *Springer Handbook of Acoustics*, T. D. Rossing, Ed. (Springer-Verlag, New York, ed. 2, 2015).
2. T. Wang *et al.*, A self-healable, highly stretchable, and solution processable conductive polymer composite for ultrasensitive strain and pressure sensing. *Adv. Funct. Mater.* **28**, 1705551 (2017).
3. Y. Chen, H. Liu, M. Reilly, H. Bae, M. Yu, Enhanced acoustic sensing through wave compression and pressure amplification in anisotropic metamaterials. *Nat. Commun.* **5**, 5247 (2014).
4. W. Li *et al.*, Sensitivity-enhanced wearable active voiceprint sensor based on cellular polypropylene piezoelectret. *ACS Appl. Mater. Interfaces* **9**, 23716–23722 (2017).
5. I. Graz *et al.*, Flexible ferroelectret field-effect transistor for large-area sensor skins and microphones. *Appl. Phys. Lett.* **89**, 073501 (2006).
6. I. Voiculescu, A. N. Nordin, Acoustic wave based MEMS devices for biosensing applications. *Biosens. Bioelectron.* **33**, 1–9 (2012).
7. J. A. Guggenheim *et al.*, Ultrasensitive plano-concave optical microresonators for ultrasound sensing. *Nat. Photonics* **11**, 714–719 (2017).
8. R. Hinchet *et al.*, Transcutaneous ultrasound energy harvesting using capacitive triboelectric technology. *Science* **365**, 491–494 (2019).
9. Y. Liu, M. Pharr, G. A. Salvatore, Lab-on-skin: A review of flexible and stretchable electronics for wearable health monitoring. *ACS Nano* **11**, 9614–9635 (2017).
10. H. Ren, H. Jin, C. Chen, H. Ghayvat, W. Chen, A novel cardiac auscultation monitoring system based on wireless sensing for healthcare. *IEEE J. Transl. Eng. Health Med.* **6**, 1900312 (2018).
11. S. M. Debbal, F. Bereksi-Reguig, Computerized heart sounds analysis. *Comput. Biol. Med.* **38**, 263–280 (2008).

12. Y. Hu, E. G. Kim, G. Cao, S. Liu, Y. Xu, Physiological acoustic sensing based on accelerometers: A survey for mobile healthcare. *Ann. Biomed. Eng.* **42**, 2264–2277 (2014).
13. P. Erne, Beyond auscultation–Acoustic cardiography in the diagnosis and assessment of cardiac disease. *Swiss Med. Wkly.* **138**, 439–452 (2008).
14. S. Cha *et al*., Porous PVDF as effective sonic wave driven nanogenerators. *Nano Lett.* **11**, 5142–5147 (2011).
15. T. Inaoka *et al*., Piezoelectric materials mimic the function of the cochlear sensory epithelium. *Proc. Natl. Acad. Sci. U.S.A.* **108**, 18390–18395 (2011).
16. H. S. Lee *et al*., Flexible inorganic piezoelectric acoustic nanosensors for biomimetic artificial hair cells. *Adv. Funct. Mater.* **24**, 6914–6921 (2014).
17. C. Dagdeviren *et al*., Conformal piezoelectric energy harvesting and storage from motions of the heart, lung, and diaphragm. *Proc. Natl. Acad. Sci. U.S.A.* **111**, 1927–1932 (2014).
18. S. Hannah *et al*., Multifunctional sensor based on organic field-effect transistor and ferroelectric poly(vinylidene fluoride trifluoroethylene). *Org. Electron.* **56**, 170–177 (2018).
19. R. Ding *et al*., High-performance piezoelectric nanogenerators composed of formamidinium lead halide perovskite nanoparticles and poly(vinylidene fluoride). *Nano Energy* **37**, 126–135 (2017).
20. H. Hu *et al*., Stretchable ultrasonic transducer arrays for three-dimensional imaging on complex surfaces. *Sci. Adv.* **4**, eaar3979 (2018).
21. A. Yu *et al*., Self-powered acoustic source locator in underwater environment based on organic film triboelectric nanogenerator. *Nano Res.* **8**, 765–773 (2015).
22. W. Li *et al*., Nanogenerator-based dual-functional and self-powered thin patch loudspeaker or microphone for flexible electronics. *Nat. Commun.* **8**, 15310 (2017).
23. S. Kang *et al*., Transparent and conductive nanomembranes with orthogonal silver nanowire arrays for skin-attachable loudspeakers and microphones. *Sci. Adv.* **4**, eaas8772 (2018).
24. L. Persano *et al*., High performance piezoelectric devices based on aligned arrays of nanofibers of poly(vinylidenefluoride-co-trifluoroethylene). *Nat. Commun.* **4**, 1633 (2013).
25. J. Chang, M. Dommer, C. Chang, L. Lin, Piezoelectric nanofibers for energy scavenging applications. *Nano Energy* **1**, 356–371 (2012).
26. C. Lang *et al*., High-output acoustoelectric power generators from poly(vinylidenefluoride-co-trifluoroethylene) electrospun nano-nonwovens. *Nano Energy* **35**, 146–153 (2017).
27. B.-S. Lee *et al*., Effects of substrate on piezoelectricity of electrospun poly(vinylidene fluoride)-nanofiber-based energy generators. *ACS Appl. Mater. Interfaces* **6**, 3520–3527 (2014).
28. C. Lang, J. Fang, H. Shao, X. Ding, T. Lin, High-sensitivity acoustic sensors from nanofibre webs. *Nat. Commun.* **7**, 11108 (2016).
29. X. Fan *et al*., Ultrathin, rollable, paper-based triboelectric nanogenerator for acoustic energy harvesting and self-powered sound recording. *ACS Nano* **9**, 4236–4243 (2015).
30. J. Yang *et al*., Triboelectrification-based organic film nanogenerator for acoustic energy harvesting and self-powered active acoustic sensing. *ACS Nano* **8**, 2649–2657 (2014).
31. T. Someya, M. Amagai, Toward a new generation of smart skins. *Nat. Biotechnol.* **37**, 382–388 (2019).
32. D. J. Lipomi *et al*., Skin-like pressure and strain sensors based on transparent elastic films of carbon nanotubes. *Nat. Nanotechnol.* **6**, 788–792 (2011).
33. J. Park *et al*., Electromechanical cardioplasty using a wrapped elasto-conductive epicardial mesh. *Sci. Transl. Med.* **8**, 344ra86 (2016).
34. Y. Liu *et al*., Epidermal mechano-acoustic sensing electronics for cardiovascular diagnostics and human-machine interfaces. *Sci. Adv.* **2**, e1601185 (2016).
35. T. Ha *et al*., A chest-laminated ultrathin and stretchable E-tattoo for the measurement of electrocardiogram, seismocardiogram, and cardiac time intervals. *Adv. Sci. (Weinh.)* **6**, 1900290 (2019).
36. D. Y. Park *et al*., Self-powered real-time arterial pulse monitoring using ultrathin epidermal piezoelectric sensors. *Adv. Mater.* **29**, 1702308 (2017).
37. C. Dagdeviren, Z. Li, Z. L. Wang, Energy harvesting from the animal/human body for self-powered electronics. *Annu. Rev. Biomed. Eng.* **19**, 85–108 (2017).
38. S. N. Cha *et al*., Sound-driven piezoelectric nanowire-based nanogenerators. *Adv. Mater.* **22**, 4726–4730 (2010).
39. S. Niu *et al*., Theory of freestanding triboelectric-layer-based nanogenerators. *Nano Energy* **12**, 760–774 (2015).
40. S. Dass, R. Jha, Micro-tip cantilever as low frequency microphone. *Sci. Rep.* **8**, 12701 (2018).
41. H. Guo *et al*., A highly sensitive, self-powered triboelectric auditory sensor for social robotics and hearing aids. *Sci. Robot.* **3**, eaat2516 (2018).
42. V. Padmanabhan, J. L. Semmlow, W. Welkowitz, Accelerometer type cardiac transducer for detection of low-level heart sounds. *IEEE Trans. Biomed. Eng.* **40**, 21–28 (1993).
43. A. Miyamoto *et al*., Inflammation-free, gas-permeable, lightweight, stretchable on-skin electronics with nanomeshes. *Nat. Nanotechnol.* **12**, 907–913 (2017).
44. S. Lee *et al*., Ultrasoft electronics to monitor dynamically pulsing cardiomyocytes. *Nat. Nanotechnol.* **14**, 156–160 (2019).